THE JOURNAL OF PHYSICAL CHEMISTRY C
A JOURNAL OF THE AMERICAN CHEMICAL SOCIETY

pubs.acs.org/JPCC

Article

Picosecond-Resolved Raman Response of a Si Nanotip for Probing Temperature and Thermal Stress in the Confined Regime under Laser Heating

Shugang Deng,[⊥] Shen Xu,[⊥] Jianshu Gao, Hao Wu, Jinjuan She, and Yanan Yue*

Cite This: *J. Phys. Chem. C* 2022, 126, 1922−1930

Read Online

ACCESS | Metrics & More | Article Recommendations

ABSTRACT: Tip-assisted lithography is a technique full of potential for nanofabrication and data storage, allowing for nanofabrication within several nanometers using the heated nanotip. Thus, the knowledge of the instantaneous thermal response of the nanotip under the laser heating is important for temperature control. In this work, a prototype of an ultrafast thermal probing method for the apex of a silicon nanotip has been achieved. Instead of obtaining an average thermal response over the entire nanotip, the temperature and thermal stress in the confined apex region of the nanotip were successfully measured in picosecond duration. Furthermore, to understand the heat transfer process in the nanotip, comparative studies were conducted on a silicon micro-cantilever and a silicon wafer, respectively. Experiment-based simulation further revealed that the equivalent thermal conductivity of the nanotip is ∼35 W/(m·K), substantiating the reduction in the thermal conductivity of nanomaterials due to the size effect. Both nonuniform laser absorption and heat transfer deterioration in the nanotip contribute to the nonuniform temperature distribution, thermal stress, and thermal deformation. This work is expected to provide important insights into the thermal response of the nanotip and an effective way for fast thermal characterization of nanomaterials.

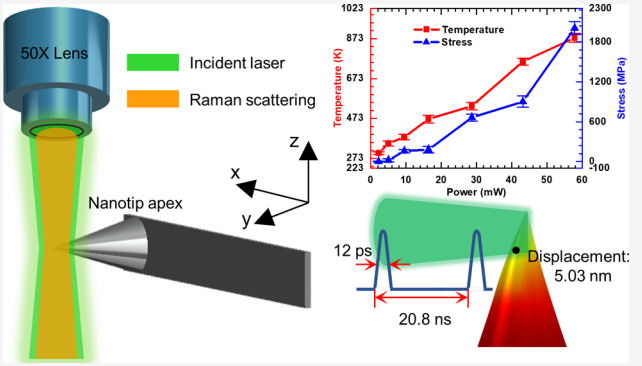

1. INTRODUCTION

One inherent limitation for traditional photolithography in material patterning is low spatial resolution caused by Abbe's diffraction limit.[1] With the development of scanning probe technology,[2−4] this undesirable issue was successfully addressed by the scanning probe lithography (SPL), which was first applied in IBM's Millipede Project[5] to achieve ultrahigh data storage density. It is the very first effective method that was recognized for imaging and shaping the surface of the specimen at the nanometer level.[6,7] Heated by integrated resistive heaters or laser irradiation, the nanotip can be used to perform diverse nanofabrication techniques, including removal, conversion, and addition, at the surface of the material. The laser-assisted one is comparatively preferable because embedding the resistive heater into a tip at the nanoscale is demanding.[8] Among the series of modulated lasers, a sub-microsecond pulsed laser is commonly employed in surface/material modification because of its intrinsic features including the high energy density, temporal resolution, and small heat-affected area.[9−11] However, simply applying the heated nanotips to material fabrication, without keeping track of its instantaneous temperature, will lead to unexpected problems in the manufacturing process because the temperature even ranges drastically for the same material with different actual needs.[6,7] Thus, figuring out the photothermal effect at the nanoscale and predicting the thermal response of the nanotips are particularly useful in temperature monitoring and adjustment. Therefore, the appropriate temperature is considered as one of the requirements for stable lithography resolution and long service life of the nanotip.[6,12]

In the SPL technique, the nanoscale fabrication is achieved by processing the specimen surface with the nanotip where a hotspot is formed at its apex. There have been plenty of simulation works[13−15] in nanotip temperature prediction and heat transfer at the nanoscale[16−18] so far, whereas the experimental studies are very limited as they are not easy to implement. This is because only the traditionally used thermocouples in the nano version would be applicable for temperature measurement at such a tiny scale. However, it is challenging in manufacturing the thermocouples and effectively

Received: November 12, 2021
Revised: December 27, 2021
Published: January 6, 2022

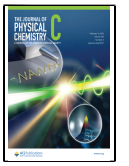

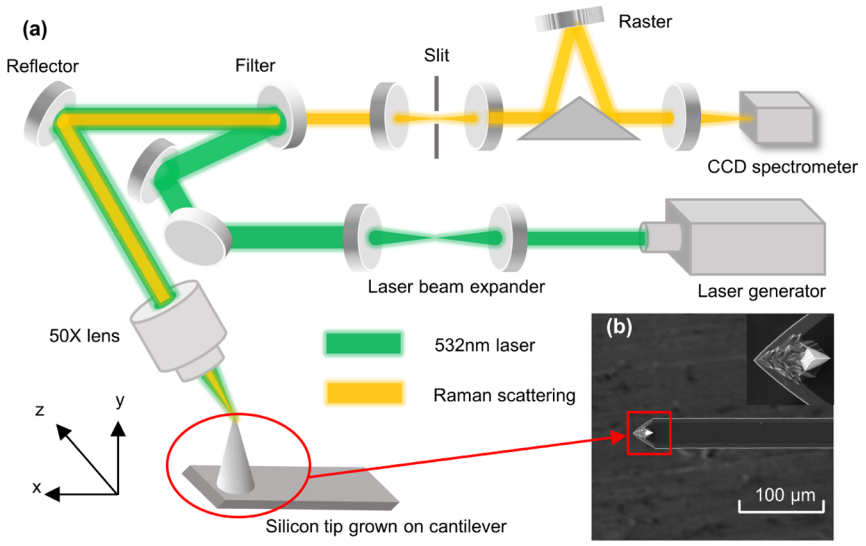

Figure 1. Schematic setup of the Raman scattering measuring system. (a) Optical path diagram for the Raman system. (b) SEM photo of the employed AFM probe. The tip grows on the end of the cantilever (350 μm × 40 μm × 3 μm). The tapered tip is 15 μm tall with a typical tip radius of 10 nm and a half cone angle of 20°.

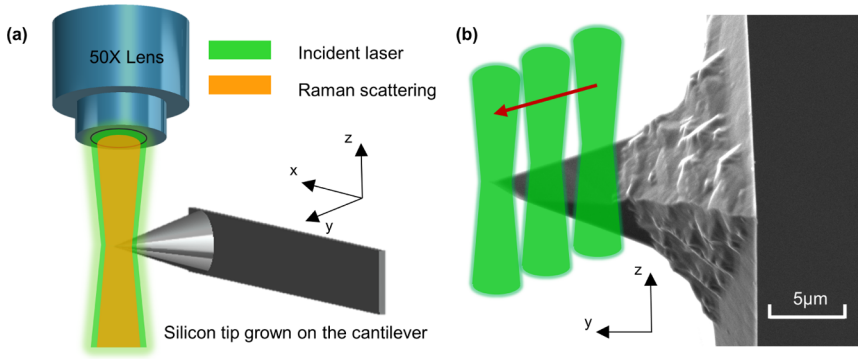

Figure 2. Determination of the tip location under the incident laser. (a) Simplified schematic of the tapered tip illuminated by the incident 532 nm laser from the side; (b) SEM photo of the tip from the side view. The incident laser moves in the direction of the red arrow and finally focuses on the tip apex.

adopting them to measure temperature at the nanoscale.[19] Besides, the response rate is determined by the thermal time constant of the thermocouples, which requires a few microseconds to acquire the temperature,[20,21] making it disadvantageous in ultrafast measurement/fabrication.

Raman thermometry, as a powerful technique, is widely used in determining the local temperature of the material at the nanoscale.[22,23] As a noncontact and nondestructive method, it provides an alternative for fragile or small-sized material detection, which has been reported in many studies in thermal measurement. Xu et al.[24] demonstrated an approach to probe the temperature rise of the multiwalled carbon nanotubes placed on Au nanoparticles using Raman thermometry. They successfully measured the temperature of the nanotubes and revealed the quasi-ballistic thermal transport in low-dimensional nanomaterials. Except for temperature measurement, the Raman method is able to probe the thermal stress in materials.[25−27] Abel et al.[28] proved the Raman spectroscopy to be a successful micro-thermometry for the micro-electro-mechanical system and presented a method to deal with absolute temperature measurement at the extreme case with submicron resolution.

In Raman thermometry, the continuous wave laser is commonly adopted because it is more accessible and its power is often set low as an individual probing source. Nowadays, ultrafast lasers are more and more introduced to manufacturing because the energy can be concentrated in a single pulse. In this work, an ultrafast Raman excitation laser was employed instead, the high-energy-density laser source was used for simultaneous heating and probing and it can be guaranteed that the Raman intensity of nanomaterials is strong enough to be precisely captured. Ultrafast lasers such as picosecond pulses show a wide range of applications in material fabrication and measurement.[29,30] Kumar et al.[31] presented a method to determine the temperature at the apex of the silicon tips with different doping levels through femtosecond pulsed laser in laser-assisted atom probe tomography. Some other researchers used the picosecond laser to probe chemistry in the tip-enhanced Raman spectroscopy with submolecular spatial resolution and higher temporal resolution.[2,32]

In this work, a picosecond Raman thermal characterization method was developed to achieve ultrafast tip heating while measuring the temperature simultaneously. In addition, this work features the nanoscale spatial resolution in thermal measurement, which enables us to study the ballistic thermal transport within the nanotip area. Under this ultrafast heating and temperature probing, the thermal stress within this confined nanoscale region was further studied to explore the size effect of

https://doi.org/10.1021/acs.jpcc.1c09771
J. Phys. Chem. C 2022, 126, 1922−1930

heat conduction and accumulation, which can aid in understanding and preventing nanostructures from heat damage.

2. EXPERIMENTAL SETUP

The experimental setup for the Raman system is shown schematically in Figure 1a. A confocal Raman microscopy from B&W TEK Company is employed to fulfill the Raman scattering collection. The excitation source includes two laser generators. It could achieve both steady state and transient laser heating/Raman excitation in the same optical path. During the experiment, the excitation laser reflects on a longpass filter, passes through the objective, and focuses on the sample surface where Raman scattering occurs. The Raman scattering from the surface is then collected by the same objective, transmitted to the spectrometer, and recorded by the thermoelectrically cooled CCD detector, which takes a wavenumber range from 0.45 to 3000 cm^{-1} with a resolution of ~2.15 cm^{-1}.

An uncoated atomic force microscopy (AFM) silicon probe from MikroMasch CSC37 was used as the sample nanotip in the experiment. Figure 1b shows its scanning electron microscopy (SEM) image performed on a field emission MIRA3 TESCAN scanning electron microscope operating at 5 kV in the lens mode. The sample was fixed on a holder attached to a three-axis translation stage, making it feasible to precisely move the nanotip at the narrow spatial area. Both the spectrometer and laser generator were connected to the computer and could be operated via the preinstalled operating system. The feedback signals were first taken by the receiver and then processed by the program affiliated to the support software.

Because the laser spot is quite large (~70 μm in diameter) at the focal level in the z direction in Figure 2a, it is necessary to carefully adjust the location of the nanotip in the $x-y$ plane, so that the laser could only be focused on the apex of the tip. Extra irradiations on the cantilever or the tip base should be avoided. Thus, the optical location of the tip under the laser was searched by moving the tip delicately as shown in Figure 2 and determined based on the Raman signal as its intensity is directly associated with the irradiated area on the sample.[33] For simplicity, all adjustments were made by referring to the coordinate system established with a resolution of 5 μm. The tip was first moved along the direction of the cantilever (i.e., x-axis) while keeping it unchanged in the other two directions. It was fixed when the strongest Raman intensity happened because this indicated that the laser exactly focused on the tip center. The tip was then adjusted along the y axis and eventually located at the place where the Raman signal can be just detected. According to the moving resolution of 5 μm for the sample stage, it is easy to infer that the surface area of roughly 5 μm from the tip apex on the tip was irradiated by the laser spot. To avoid the heating effect on the nanotip, the lowest laser power (~2 mW) was used in the coordinate adjustment.

3. RESULTS AND DISCUSSION

3.1. Calibration Results. Temperature measurement by the Raman method was based on the changes in the Raman peak, such as Raman shift and linewidth. The Raman shift-based temperature measurement might be affected by the presence of thermal stress, while the linewidth is preferred to provide with an absolute measurement of temperature due to its stress insensitivity. The parabolic relationship between the linewidth and material temperature is approximated as

$$\Gamma = A(T_\Gamma - T_0)^2 + B(T_\Gamma - T_0) + \Gamma_0 \quad (1)$$

where Γ is the linewidth of the Raman peak, T_Γ is the unbiased linewidth-based temperature, T_0 is the linewidth at room temperature, and A and B are the parameters to be calibrated. Though the linear relationship between Raman linewidth and temperature was widely adopted in the previous work, a curvilinear relationship could better describe the changing trend of Raman linewidth against temperature in a wide temperature range from room temperature to several hundreds of degree Celsius.[34,35]

Specifically, the definition of the Raman shift depends on the existence of thermal stress. For the Raman peak without the stress effect, the Raman shift is described by eq 2, whereas the Raman shift is determined by eq 3 if the Raman peak comes with the stress effect

$$\omega = C(T_\omega - T_0) + \omega_0 \quad (2)$$

$$\omega = C(T_\omega - T_0) + D\sigma + \omega_0 \quad (3)$$

where ω is the measured Raman shift of the Raman peak, σ is the average stress, ω_0 is the Raman shift at room temperature, T_ω is the Raman shift-based temperature, while T_0 is the room temperature, and C and D are the parameters to be determined.

Theoretically, T_ω equals to the linewidth-based temperature T_Γ if there is no stress in the material. However, the stress exists and could not be neglected in most cases. It is then defined as a function of the difference between T_ω and T_Γ as following

$$\sigma = \frac{(T_\omega - T_\Gamma)C}{D} \quad (4)$$

It is obvious that compressive stress will result in an underprediction of the Stokes peak-based temperature ($T_\omega < T_\Gamma$), while tensile stress will induce an overprediction of the Stokes peak-based temperature ($T_\omega > T_\Gamma$).

Raman spectrometer with an excitation wavelength of 532 nm was used to probe the thermal response of silicon materials. According to Doerk et al.,[36] specimen size shows no effect on the linear temperature dependence of Raman shift in silicon materials. Therefore, a silicon wafer can be employed in the calibration experiment. The temperature of the wafer was adjusted using a heating sheet by changing the electric current applied to it. A thermocouple was attached to the silicon wafer to monitor the temperature simultaneously. During the calibration, the laser power for probing was set as low as possible to minimize heating effects.

A typical Raman spectrum for silicon has a featured peak centered at ~520 cm^{-1} at room temperature. The peak shifts gradually to the left (redshift) when the temperature is rising, as illustrated in Figure 3a. A Lorentzian fitting was further performed on each spectrum to determine the precise Raman shift and linewidth. The best parabolic fitting result for the curve of the linewidth against temperature was used to determine the parameters A and B and the best linear fitting result for the Raman shift for parameter C (slope of the fitting line). According to Wolf,[37] the thermal stress-related constant D = −3.6 cm^{-1}/GPa was used in the following calculation. All the parameters are summarized in Table 1.

3.2. Thermal Responses of the Nanotip under Continuous Laser Heating. Under the continuous-wave (CW, 532 nm) laser irradiation, a steady-state heat transfer could be first established for the nanotip. Because the total height of the tip is ~15 μm smaller than the diameter of the laser spot, only part of the laser spot covered the tip surface (~5 μm near the tip apex). A comparative experiment was conducted on

https://doi.org/10.1021/acs.jpcc.1c09771
J. Phys. Chem. C 2022, 126, 1922−1930

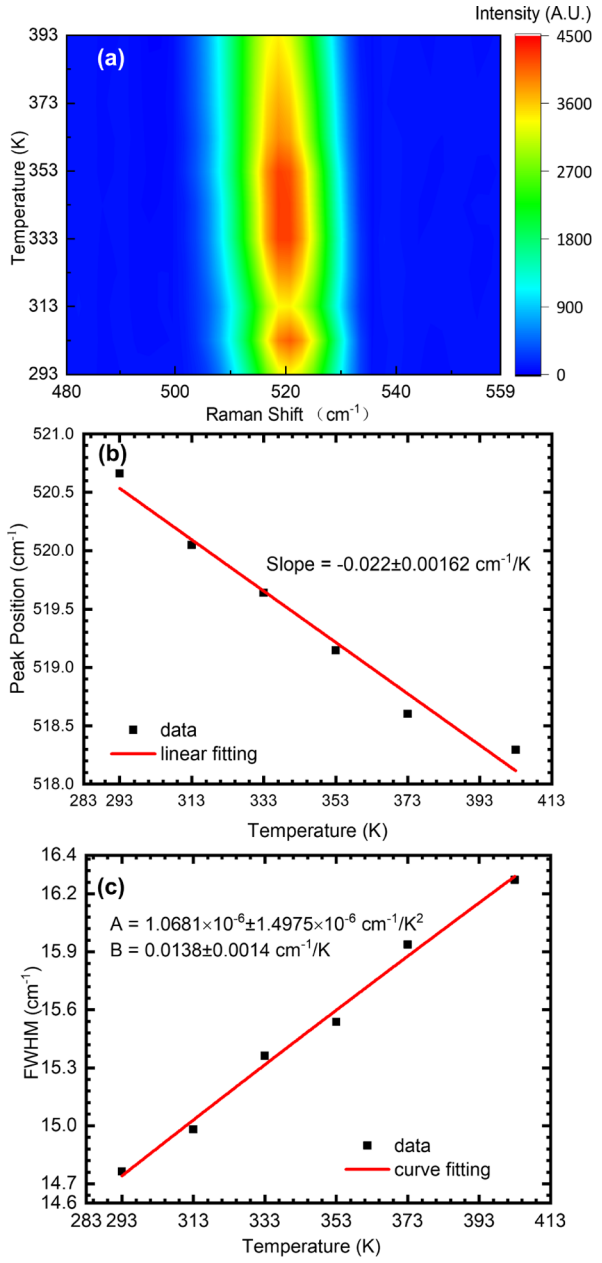

Figure 3. Raman characterization calibration results of silicon. (a) Raman peak shifts linearly to the left as temperature rises; (b) Raman peak position (ω) of silicon at different temperatures. The Raman peak moves to the left as the temperature rises. The peak position shows a linear relationship with temperature and the slope of the fitting line represents the value of C in eq 2; (c) Raman linewidth (fwhm: Γ) of silicon materials at different temperatures. The linewidth broadens as the specimen temperature increases and shows a parabolic relationship with temperature.

Table 1. Calibration Parameters Calculating Biaxial Stress and Temperature

equation	values of the parameters
eq 1	$A = 1.0681 \times 10^{-6} \pm 1.4975 \times 10^{-7}$ cm^{-1}/K^2
	$B = 0.0138 \pm 0.0014$ cm^{-1}/K
eq 3	$C = -0.022 \pm 0.0016$ cm^{-1}/K
	$D = -3.6$ cm^{-1}/GPa (ref 33)

the cantilever and silicon wafer to analyze the size effect on the steady-state heating. To minimize the measurement error, every result Raman spectrum under each laser power was obtained by averaging three repeated measurements with an integration time of 20 s for each. Using eqs 1 and 4, the absolute temperature and thermal stress were determined from the Raman shift and linewidth of the 520 cm^{-1} peak using the Lorentzian fitting.

Subplots in Figure 4 illustrate how the temperature and thermal stress change over the different designated CW laser powers (i.e., 2, 4, 6, 8, and 10 mW). The temperature of the tip apex and cantilever reached ~329 and ~311 K, respectively, under the power of 10 mW, whereas silicon wafer could only be heated to ~299 K in the same condition. The difference in the temperature rise of the different samples could be attributed to several reasons. From the perspectives of heat conduction, the nanotip had the largest heat conduction resistance due to its tip shape, and the wafer has the lowest heat conduction resistance. Thus, under the same heat flux, the nanotip has the highest temperature rise. The different orders of magnitude in size would also raise the size effect on the effective thermal conductivity, especially for the nanotip. The phonon confinement happened in the nanotip. The strong scattering of the phonons at the boundary would largely reduce the effective thermal conductivity of the nanotip.[38] In addition to the heat conduction, heat convection occurred at the same time as the temperature rose. The convective coefficient for the nanotip would be significantly increased because of its nanometer size (detailed in later section). Though the heat convection over the nanotip enhanced the heat transferring from the tip apex, the tradeoff between heat conduction limitation and heat convection enhancement still resulted in the highest temperature rise in the nanotip among three samples.

For the micro-cantilever and silicon wafer, the size of all three dimensions of two structures is larger than the silicon phonon mean free path. The heat conduction process would obey the Fourier's law, and the effective thermal conductivity was close to the bulk value. The difference in the temperature rise would be mainly caused by the different heat conduction resistances. The cantilever has a higher heat conduction resistance than the wafer due to its beam shape when the heat conducts along the length of the cantilever.

The obvious tensile stress of ~130 MPa was observed on the tip apex when heated by the CW laser at the power of 10 mW. This could be attributed to the high temperature rise and steep temperature gradient in the nanotip, while the stress change in silicon wafer almost remained constant over the increase in laser power. Theoretically, the tensile stress will keep increasing when the temperature of the material rises. However, the wafer indicates, interestingly, the sign of being compressed in the irradiated area. This compressive stress identified in bulk silicon is probably caused by the unequal thermal expansions of the unirradiated area and irradiated part.

3.3. Thermal Responses of the Nanotip with Picosecond Pulse Excitation. As in SPL, only a small volume at the nanometer scale in materials will be heated under the nanotip, the modification will last just a few nanoseconds. The transient thermal state of the nanotip in an even shorter duration than nanosecond is critical. Thus, a picosecond laser (532 nm with the pulse duration of 12 ps and the repetition rate of 48 MHz) was then introduced to probe the transient-state thermal transport in the three samples. Raman scatterings were excited within the laser pulse duration (12 ps) and simultaneously collected by the spectrometer. The temperature rises on the tip

https://doi.org/10.1021/acs.jpcc.1c09771
J. Phys. Chem. C 2022, 126, 1922−1930

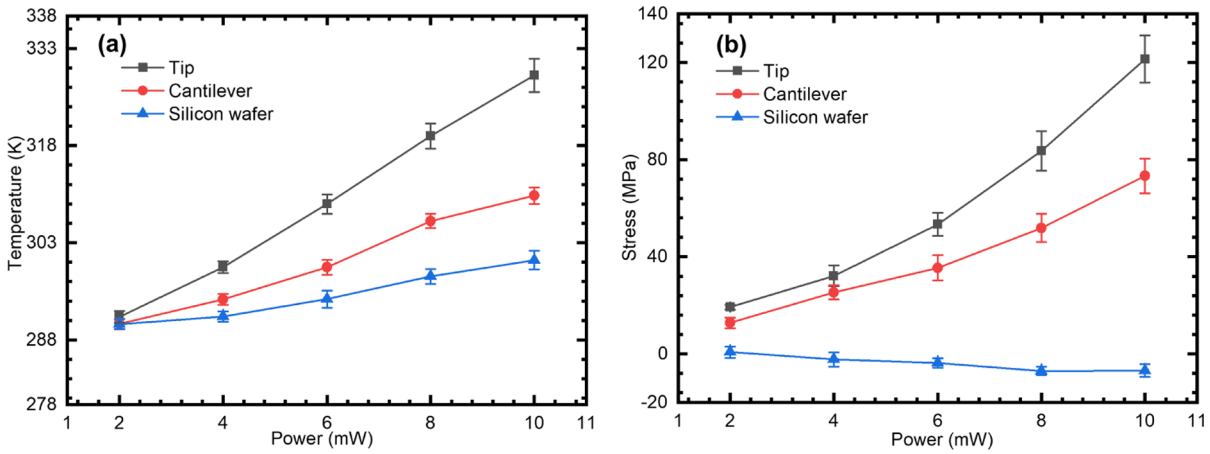

Figure 4. Thermal characterization of the three specimens under CW laser irradiation. (a) Temperature rise of the tip, cantilever, and wafer under continuous wave laser of different powers; (b) thermal stress of the tip, cantilever, and wafer under continuous-wave laser of different powers. The laser illuminates the tip apex instead of the entire tip in the experiment.

apex under different laser powers are presented in Figure 5a to the right axis. Similar to the steady-state result, the greatest temperature rise occurred on the tip apex among the three structures. Being irradiated by the incident laser of 57.8 mW, the temperature of the tip rose to 876 ± 28 K. The result was averaged from five times repeated measurements. The stress over the apex was derived based on the linewidth-based and peak-based temperatures and is plotted against the incident power in Figure 5a to the left axis. As expected, the thermal stress increased as the temperature raised. The maximum thermal stress of 2007 ± 122 MPa was observed at the highest temperature, which is the same order of magnitude as it in the empirical study.[39] The nanoscale size of the tip apex and nonuniform heating contribute to nonuniform temperature distribution, which leads to excessive thermal gradients and thermal stress in the tip.

Comparative experiments on the cantilever and silicon wafer were conducted to study the size effect on the thermal transport under the ps laser. Temperature and stress for the cantilever are shown in Figure 5b. The temperature and thermal stress of the cantilever rose to 491 ± 8 K and 1566 ± 57 MPa, respectively, under the strongest pulse power irradiation. While the variation trend of the temperature over the tip apex and cantilever are similar to each other, the temperature rise of the latter one is slightly lower. It is notable that Raman scatterings were only collected in the pulse duration (∼12 ps). During such an ultrafast period, the most generated heat was mainly accumulated in the irradiated volume rather than conducted to the low-temperature region because heat could be conducted over a small distance less than ∼100 nm. Another possible reason is that the micro-cantilever has the higher thermal conductivity and wider convective heat transfer area than the nanotip apex, which will be discussed later.

Figure 5c presents how the temperature of the silicon wafer varies over the laser power. The highest temperature detected is 376 ± 6 K, which is way less than that on the surface of the tip apex or cantilever. Interestingly, greater compressive stress was observed in the silicon wafer when it is heated by the pulsed laser. The greatest stress reached −158 ± 9 MPa at the highest temperature. While we observed the incremental tensile stress on the tip apex and cantilever along with the rising temperature, the increasing compressive stress is otherwise detected on the wafer. This phenomenon has also been reported in previous works.[40−42] When measuring the silicon wafer, the laser focuses at the center and creates a hot region. The hot region tends to expand but is restricted by the neighboring low-temperature region leading to stress inward the hot region. On the contrary, the size of the tip apex and cantilever is smaller than the laser spot, so they can be fully covered by the incident beam. Thus, tensile stress is detected in the tip apex and cantilever, which is caused by the tensile force from the low-temperature region when the heated region is free to expand.

For the semiconductor silicon under irradiation of the 532 nm laser, multiple physical processes will occur because the incident photon energy (∼2.33 eV) is more than twice higher than the band gap of the single crystal silicon (∼1.1 eV at room temperature). The processes include excitation of electron−hole pairs, thermalization of "hot" electrons and holes, excess carrier diffusion, recombination, thermal energy transfer to the lattice (phonon), and phonon diffusion. For the silicon wafer, the heat transfer and carrier diffusion processes could be respectively described using Meyer et al.'s model,[43,44] in which only the diffusion in the depth direction is considered due to the large spot size. The temperature, T, and carrier density, n, are given by

$$\frac{\partial T}{\partial t} - \frac{\partial}{\partial z}\left[\alpha(n, T)\frac{\partial T}{\partial z}\right] = \frac{G(n, T, z, t)}{\rho c_p(T)} \tag{5}$$

$$\frac{\partial n}{\partial t} - \frac{\partial}{\partial z}\left[D(n, T)\frac{\partial n}{\partial z}\right] = g(n, T, z, t) - \frac{(n - n_i)}{\tau_B(n, T)} \tag{6}$$

where z is the depth into the wafer and t is the time. The thermal diffusivity α, which is the function of thermal conductivity k, mass density ρ, and specific heat of silicon c_p, follows $\alpha = k/\rho c_p$. G is the rate of heat generation, D is the ambipolar diffusion coefficient, g is the rate of excess carrier generation, n_i is the intrinsic carrier concentration, and τ_B is the bulk free carrier lifetime. The boundary conditions applied to eqs 5 and 6 include

https://doi.org/10.1021/acs.jpcc.1c09771
J. Phys. Chem. C 2022, 126, 1922−1930

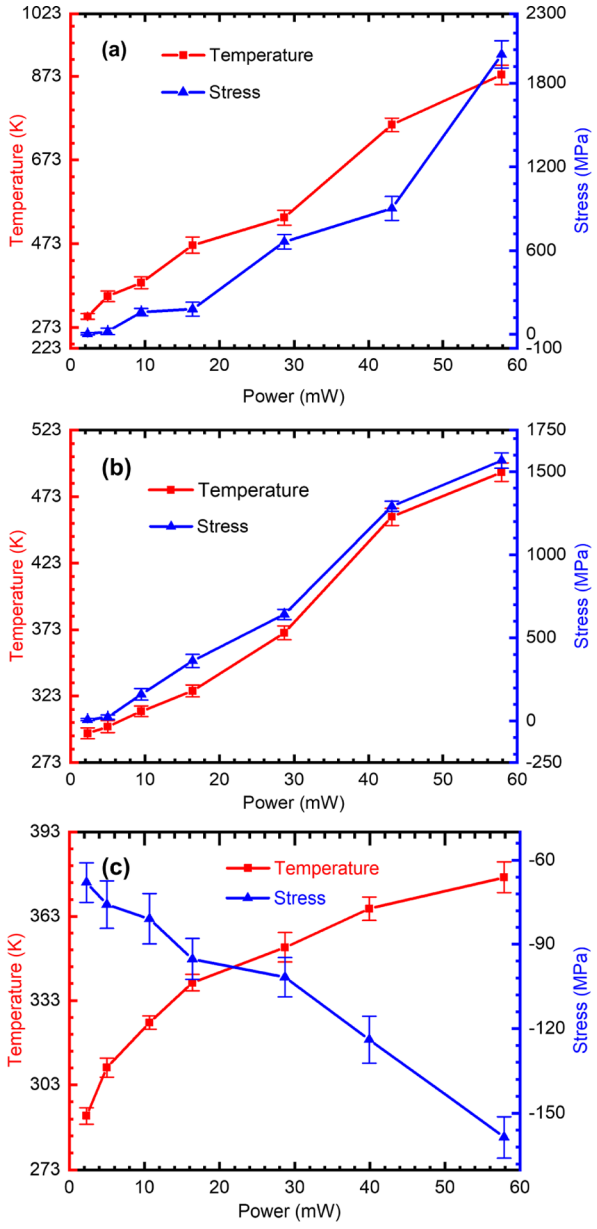

Figure 5. Thermal response of the three specimens excitated by picosecond laser. (a) Temperature and thermal stress of the tip apex under picosecond laser of different powers; (b) temperature and thermal stress of the cantilever under picosecond laser of different powers; and (c) temperature and thermal stress of the silicon wafer under picosecond laser of different powers. The error bar is the standard deviation for five measurements.

$$
\begin{aligned}
&T(z, t = 0) = T_0,\\
&T(z = \infty, t) = T_0,\\
&n(z, t = 0) = n_i(T_0),\\
&n(z = \infty, t) = n_i(T_0),\\
&k\frac{\partial T}{\partial z} + G_s|_{z=0} = 0,\\
&D\frac{\partial n}{\partial z} - s(n - n_i)|_{z=0} = 0
\end{aligned}
\tag{7}
$$

where T_0 is the initial specimen temperature, G_s is the rate of heat generation at the surface, and s is the surface recombination velocity.

Given the abovementioned processes happen together, an effective heating depth L_H was proposed to correlate the incident energy and surface temperature rise and roughly interpreted the overall heating effect in the semiconductor.[43] Functionally, L_H follows

$$
L_H = \frac{E_0[1 - R(T_0)]}{\rho c_p(T_0)\Delta T} \tag{8}
$$

where E_0 is the energy density of incidence, ΔT is the temperature rise, and R is the reflectivity (~0.35 for Si). Substituting our experimental parameters and measured temperature rise of the silicon wafer, the effective heating depth L_H is determined to be from 1.1×10^{-7} to 2.6×10^{-7} m along with the increment of the incident energy density. The result is consistent with the reported result in[37] on both the order of magnitude and varying trend of L_H. Although the model above is not applicable for the heat transfer and diffusion in the cantilever because of its structure, the physical processes are similar. As the commercial AFM tips are usually manufactured by using the wet-etching method, it will increase the roughness of the surface and enhance the optical absorption coefficient at the irradiated side, which will result in a slightly higher temperature rise in the cantilever than in the wafer. Because the tip width is much smaller than the determined heating length in the crystalline silicon and the enhanced optical field is trapped inside the tip at the irradiated side,[45] the highest temperature rise can be therefore observed at the tip as the incident energy is highly concentrated within a small region. Besides, the size of the tip at the nanoscale significantly confines the diffusion of carriers, which makes the temperature rise increase linearly along with the incident energy increase.

3.4. Simulation of the Nanotip Heated by Picosecond Pulses. To better understand the heat transfer over the tip apex, the finite element method (FEM) was employed for the time-domain transient analysis of the heating process by the picosecond laser. For simplicity, the tip was approximated to be a circular cone on the end of the cantilever. Figure 6a shows the shape and the direction of the incident laser. The parameters of the input laser used in the model are listed in Table 2. To closely match the experiment conditions, an inward heat flux was introduced to the tip from a side within 5 μm zone near its apex. The absorption of the incident photon energy by the Si tip was calculated in advance by using the finite difference time domain method. Because this sample tip was etched from pure single crystalline silicon, the optical properties of pure silicon were employed in the calculation and the resulted optical absorption of the tip at the wavelength of 532 nm was approximate 0.48, which was then applied to the FEM simulation. The switch of high heat load resolution was managed by the two explicit events added so that the overall computational cost could be minimized. The subplot in Figure 6a presents the meshes near the apex, which were refined to increase the accuracy of the solution.

Besides heat conduction, the convective thermal transport at the nanoscale is quite different from that at the macroscale. The increase of the surface-to-volume ratio is considered as the main contributor to the enhancement of heat convection at the micro-/nanoscale. Its value has been proven to be several orders of magnitude greater than that at the macroscale.[46] There are

https://doi.org/10.1021/acs.jpcc.1c09771
J. Phys. Chem. C 2022, 126, 1922−1930

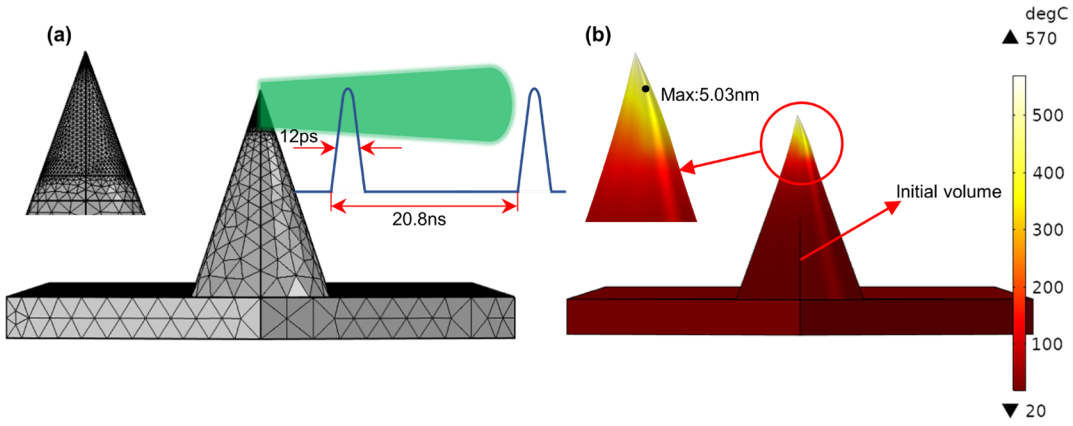

Figure 6. Simulation of the tip excited by picosecond pulses. (a) Geometric model of the tapered tip grown on the cantilever. The tip is illuminated by the incident pulses with a duration time of 12 ps from the right side. The laser-irradiated area is 5 μm near the apex, where the meshes are refined. (b) Simulation result of the tip temperature distribution under picosecond pulse excitation.

Table 2. Input Laser Parameters Used in the Model

designation	symbol	value used in the model
laser spot radius	r_{spot}	35 μm
average power	P_{ave}	57.8 mW
pulse duration	τ	12 ps
frequency of laser pulses	f	48 MHz
laser power during the pulse	P_{laser}	≈100.35 W

three classes of flow regimes. The types which are specified based upon the thresholds of their Knudsen number Kn (the ratio between the mean free path of the gas molecules and the characteristic length) are as follows: (i) continuum regime when $Kn < 0.01$; (ii) transition regime when $0.01 < Kn < 10$; and (iii) free molecular regime when $Kn > 10$. Following Wang et al.[47] and Klein et al.,[48] we found the transition regime near the tip apex because the Knudsen number was $0.011 < Kn < 5.9$ in the irradiated area. The convection heat transfer coefficient h keeps decreasing as the material diameter increases in the transition regime. To simplify our analysis while maintaining their correlation, the coefficient h was therefore approximated to the function of material diameter in our simulation as $h \approx 8000/[1 + (d/75)^{1.12}] + 3000$, where d is the diameter in nanometers.

Figure 6b illustrates the simulation result of temperature distribution across the tip under the treatment of 57.8 mW picosecond-pulsed laser. To make sure of the convergence of the simulated result, we adjusted the total simulation time to 100 cycles with 20.8 ns for each. The thermal conductivity of the tip was then modified to make the simulated temperature equal to that measured in our experiment. Based on our works, the equivalent thermal conductivity is ∼35 W/(m·K) for the entire tip. The thermal conductivity diminishing throughout nanomaterials has already been reported in previous works. According to Ju[49] an approximate relationship between the thermal conductivity of columnar silicon material and its diameter is $k_{wire} = Cv_g[3(\Lambda_{bulk}^{-1} + d_{wire}^{-1})]^{-1}$, where Cv_g is the product of silicon heat capacity and phonon group velocity, Λ_{bulk} is the phonon mean free path with the value of ∼250 nm in bulk silicon, and k_{wire} is the thermal conductivity of the silicon wire with a diameter of d_{wire}. The thermal conductivity of the apex part with a diameter of 20 nm is only 10.8 W/(m·K) according to Ju's equation, which is an order of magnitude less than that of bulk silicon. Other factors such as rough surface will also affect the thermal conductivity,[50−52] as it further deteriorates the heat transfer. Apart from thermal conductivity reduction, an obvious thermal expansion occurred at the apex because the black wireframe (see Figure 6b) which represents the initial position and volume of the tip is no longer observable, indicating that the heated apex was out of its original shape. The maximum displacement in the nanotip apex is ∼5.03 nm, which is in the same direction as the incident laser. Both nonuniform laser heating and heat transfer deterioration contribute to the nonuniform temperature distribution over the tip, which corresponds to thermal expansion and deformation in it.

3.5. Thermal Conductivity and Heat Accumulation. As discussed in the simulation section, the effective thermal conductivity of the nanotip has been evaluated using FEM on the basis of the experimental data. The thermal conductivity, as an input parameter in the simulation, was then adjusted to make the simulated temperature similar to the experiment result. The resulted thermal conductivity of the nanotip is in the same order of magnitude as other studies, and the reduction explains the significant heat accumulation. Heat convection coefficient at the nanoscale is proven several orders of magnitude greater than that at the macroscale. Therefore, the enhancement of the convection heat transfer near the nanotip apex has been strictly considered due to the increase in surface-to-volume ratio at the nanoscale. The nanotip still showed significant temperature rise with a convection heat transfer coefficient much greater than that for the cantilever and silicon wafer. The possible reason for this is the limited convective area near the nanotip apex, which is a limitation for effective convection heat transfer. According to the experiment and simulation, it could be concluded that thermal conduction dominated the heat transfer near the nanotip apex.

For the nanotip under pulsed laser heating, heat accumulation should be significantly taken into consideration. Based on the effective heating depth L_H (from 1.1×10^{-7} to 2.6×10^{-7} m along with the increment of the incident energy density), the nanotip width is much smaller and the enhanced optical field is trapped inside the tip at the irradiated side. The thermal diffusivity α, which is the function of thermal conductivity k, mass density ρ, and specific heat of silicon c_p, follows $\alpha = k/\rho c_p$. The reduction in thermal conductivity results in the heat diffusion deterioration and further causes heat accumulation in the nanotip. Besides, the chemical etch induced surface roughness of the nanotip might also enhance the optical absorption at the irradiated side, which will result in the highest

https://doi.org/10.1021/acs.jpcc.1c09771
J. Phys. Chem. C 2022, 126, 1922−1930

temperature rise in the nanotip as the incident energy is highly concentrated within a small region. Besides, the size of the tip at the nanoscale significantly confines the diffusion of carriers, which makes the temperature rise increase linearly along with the incident energy increase.

4. CONCLUSIONS

In summary, a fast, simple, and instantaneous thermal characterization technique has been introduced for the real-time measurement of nano-/microstructures. This ultrafast Raman-based method allows for the thermal measurement of the nanotip with better temporal resolution. By some calibration and analysis of experimental data, the absolute temperature and thermal stress can be derived from the changes in the Raman peak position and linewidth. Further experiments are conducted on the cantilever and silicon wafer for comparison and explore the size effect on material heating. Under the same laser, a significant temperature rise is observed in the tip apex and cantilever, while that in bulk silicon is not so obvious. As for thermal-induced stress, worth mentioning is the compressive thermal stress detected in the wafer, which is different from the tensile stress in the tip apex and cantilever. This is probably because the tip apex and cantilever, smaller than the laser spot size, are free to expand under laser heating, but the high-temperature region is restricted by the neighboring low-temperature region leading to compressive stress in the silicon wafer. A simulation is proposed to analyze the reduction in thermal conductivity of the tip, and an equivalent thermal conductivity is estimated ∼35 W/(m·K) according to experimental data, which is 1 order of magnitude smaller than bulk silicon. The temperature and thermal stress in the tip apex are probed by our picosecond Raman thermometry, and it is found that the heat is more likely to accumulate due to the size effect and a significant tensile stress is caused by nonuniform temperature distribution in the nanotip.

AUTHOR INFORMATION

Corresponding Author

Yanan Yue − *Key Laboratory of Hydraulic Machinery Transients (MOE), School of Power and Mechanical Engineering, Wuhan University, Wuhan, Hubei 430072, China; Department of Mechanical and Manufacturing Engineering, Miami University, Oxford, Ohio 45056, United States;* orcid.org/0000-0002-3489-3949; Email: yyue@whu.edu.cn

Authors

Shugang Deng − *Key Laboratory of Hydraulic Machinery Transients (MOE), School of Power and Mechanical Engineering, Wuhan University, Wuhan, Hubei 430072, China*

Shen Xu − *School of Mechanical and Automotive Engineering, Shanghai University of Engineering Science, Shanghai 201620, China*

Jianshu Gao − *Key Laboratory of Hydraulic Machinery Transients (MOE), School of Power and Mechanical Engineering, Wuhan University, Wuhan, Hubei 430072, China*

Hao Wu − *Key Laboratory of Hydraulic Machinery Transients (MOE), School of Power and Mechanical Engineering, Wuhan University, Wuhan, Hubei 430072, China*

Jinjuan She − *Department of Mechanical and Manufacturing Engineering, Miami University, Oxford, Ohio 45056, United States*

Complete contact information is available at: https://pubs.acs.org/10.1021/acs.jpcc.1c09771

Author Contributions

⊥S.D. and S.X. contributed equally to this work and are co-first authors. Y.Y. conceived the idea. H.W. and J.S. helped S.D. to design and construct the setup. S.D. carried out all the characterization and measurements. S.X. and J.G. conducted the finite element modeling and analysis. S.D. and S.X. wrote the paper with the help of all authors. The research was carried out under the supervision of Y.Y.

Notes

The authors declare no competing financial interest.

ACKNOWLEDGMENTS

The authors acknowledge the financial support from the National Key Research and Development Program (no. 2019YFE0119900), National Natural Science Foundation of China (nos. 52076156 & 52106220), and Fundamental Research Funds for the Central Universities (no. 2042020kf0194). The authors appreciate the support from the Supercomputing Center of Wuhan University.

REFERENCES

(1) Falcón Casas, I.; Kautek, W. Subwavelength Nanostructuring of Gold Films by Apertureless Scanning Probe Lithography Assisted by a Femtosecond Fiber Laser Oscillator. *Nanomaterials* **2018**, *8*, 536.

(2) Pozzi, E. A.; Sonntag, M. D.; Jiang, N.; Chiang, N.; Seideman, T.; Hersam, M. C.; Van Duyne, R. P. Ultrahigh Vacuum Tip-Enhanced Raman Spectroscopy with Picosecond Excitation. *J. Phys. Chem. Lett.* **2014**, *5*, 2657−2661.

(3) Verma, P. Tip-Enhanced Raman Spectroscopy: Technique and Recent Advances. *Chem. Rev.* **2017**, *117*, 6447−6466.

(4) Tarun, A.; Hayazawa, N.; Yano, T.-A.; Kawata, S. Tip-Heating-Assisted Raman Spectroscopy at Elevated Temperatures. *J. Raman Spectrosc.* **2011**, *42*, 992−997.

(5) Vettiger, P.; Cross, G.; Despont, M.; Drechsler, U.; Durig, U.; Gotsmann, B.; Haberle, W.; Lantz, M. A.; Rothuizen, H. E.; Stutz, R.; et al. The "Millipede" - Nanotechnology Entering Data Storage. *IEEE Trans. Nanotechnol.* **2002**, *1*, 39−55.

(6) Howell, S. T.; Grushina, A.; Holzner, F.; Brugger, J. Thermal Scanning Probe Lithography—a Review. *Microsyst. Nanoeng.* **2020**, *6*, 21.

(7) Garcia, R.; Knoll, A. W.; Riedo, E. Advanced Scanning Probe Lithography. *Nat. Nanotechnol.* **2014**, *9*, 577−587.

(8) Lee, C. S.; Nam, H.-J.; Kim, Y.-S.; Jin, W.-H.; Cho, S.-M.; Bu, J.-u. Microcantilevers Integrated with Heaters and Piezoelectric Detectors for Nano Data-Storage Application. *Appl. Phys. Lett.* **2003**, *83*, 4839−4841.

(9) Falcón Casas, I.; Kautek, W. Subwavelength Nanostructuring of Gold Films by Apertureless Scanning Probe Lithography Assisted by a Femtosecond Fiber. *Laser Oscillator* **2018**, *8*, 536.

(10) Kozlov, A. A.; Lambropoulos, J. C.; Oliver, J. B.; Hoffman, B. N.; Demos, S. G. Mechanisms of Picosecond Laser-Induced Damage in Common Multilayer Dielectric Coatings. *Sci. Rep.* **2019**, *9*, 607.

(11) Pozzi, E. A.; Goubert, G.; Chiang, N.; Jiang, N.; Chapman, C. T.; McAnally, M. O.; Henry, A.-I.; Seideman, T.; Schatz, G. C.; Hersam, M. C.; et al. Ultrahigh-Vacuum Tip-Enhanced Raman Spectroscopy. *Chem. Rev.* **2017**, *117*, 4961−4982.

(12) Hamann, H. F.; O'Boyle, M.; Martin, Y. C.; Rooks, M.; Wickramasinghe, H. K. Ultra-High-Density Phase-Change Storage and Memory. *Nat. Mater.* **2006**, *5*, 383−387.

(13) Chapuis, P.-O.; Greffet, J.-J.; Joulain, K.; Volz, S. Heat Transfer between a Nano-Tip and a Surface. *Nanotechnology* **2006**, *17*, 2978−2981.
(14) Li, C.; Zhang, L.; Li, Y.; Wang, X. Material Behavior under Extreme Domain Constraint in Laser-Assisted Surface Nanostructuring. *Phys. Lett. A* **2016**, *380*, 753.
(15) Vella, A.; Shinde, D.; Houard, J.; Silaeva, E.; Arnoldi, L.; Blum, I.; Rigutti, L.; Pertreux, E.; Maioli, P.; Crut, A.; et al. Optothermal Response of a Single Silicon Nanotip. *Phys. Rev. B* **2018**, *97*, 075409.
(16) McCarthy, B.; Zhao, Y.; Grover, R.; Sarid, D. Enhanced Raman Scattering for Temperature Measurement of a Laser-Heated Atomic Force Microscope Tip. *Appl. Phys. Lett.* **2005**, *86*, 111914.
(17) Wang, X.; Qin, Y.; Wang, B.; Zhang, L.; Shen, Z.; Lu, J.; Ni, X. Numerical and Experimental Study of the Thermal Stress of Silicon Induced by a Millisecond Laser. *Appl. Opt.* **2011**, *50*, 3725−3732.
(18) Wang, X. Thermal and Thermomechanical Phenomena in Picosecond Laser Copper Interaction. *J. Heat Transfer* **2004**, *126*, 355−364.
(19) Zhou, M.; Kulenovic, R.; Laurien, E.; Kammerer, M.; Schuler, X. Investigation on Temperature Fluctuations in Thermal Mixing Pipe Flows by Micro-Thermocouple Measurements. *The 11th International Topical Meeting on Nuclear Reactor Thermal Hydraulics, Operation and Safety, Gyeongju, Korea*, 2016.
(20) Bourg, M. E.; van der Veer, W. E.; Grüell, A. G.; Penner, R. M. Electrodeposited Submicron Thermocouples with Microsecond Response Times. *Nano Lett.* **2007**, *7*, 3208−3213.
(21) Li, T.; Shi, T.; Tang, Z.; Liao, G.; Duan, J.; Han, J.; He, Z. Real-Time Tool Wear Monitoring Using Thin-Film Thermocouple. *J. Mater. Process. Technol.* **2021**, *288*, 116901.
(22) Wang, R.; Xu, S.; Yue, Y.; Wang, X. Thermal Behavior of Materials in Laser-Assisted Extreme Manufacturing: Raman-Based Novel Characterization. *Int. J. Extreme Manuf.* **2020**, *2*, 032004.
(23) Bergler, M.; Cvecek, K.; Werr, F.; Brehl, M.; De Ligny, D.; Schmidt, M. Cooling Rate Calibration and Mapping of Ultra-Short Pulsed Laser Modifications in Fused Silica by Raman and Brillouin Spectroscopy. *Int. J. Extreme Manuf.* **2020**, *2*, 035001.
(24) Xu, Y.; Zhao, X.; Li, A.; Yue, Y.; Jiang, J.; Zhang, X. Plasmonic Heating Induced by Au Nanoparticles for Quasi-Ballistic Thermal Transport in Multi-Walled Carbon Nanotubes. *Nanoscale* **2019**, *11*, 7572−7581.
(25) Kang, Y.; Qiu, Y.; Lei, Z.; Hu, M. An Application of Raman Spectroscopy on the Measurement of Residual Stress in Porous Silicon. *Opt Laser. Eng.* **2005**, *43*, 847−855.
(26) Wu, X.; Yu, J.; Ren, T.; Liu, L. Micro-Raman Spectroscopy Measurement of Stress in Silicon. *Microelectron. J.* **2007**, *38*, 87−90.
(27) Ashitkov, S. I.; Komarov, P. S.; Struleva, E. V.; Agranat, M. B.; Kanel, G. I. Mechanical and Optical Properties of Vanadium under Shock Picosecond Loads. *JETP Lett.* **2015**, *101*, 276−281.
(28) Abel, M. R.; Wright, T. L.; King, W. P.; Graham, S. Thermal Metrology of Silicon Microstructures Using Raman Spectroscopy. *IEEE Trans. Compon. Packag. Technol.* **2007**, *30*, 200−208.
(29) Bieda, M.; Siebold, M.; Lasagni, A. F. Fabrication of Sub-Micron Surface Structures on Copper, Stainless Steel and Titanium Using Picosecond Laser Interference Patterning. *Appl. Surf. Sci.* **2016**, *387*, 175−182.
(30) Wang, H.; Zhao, K.; Shen, H.; Yao, Z. Experimental Study on Direct Fabrication of Micro Channel on Fused Silica by Picosecond Laser. *J. Manuf. Process.* **2020**, *55*, 87−95.
(31) Kumar, A.; Bogdanowicz, J.; Demeulemeester, J.; Bran, J.; Melkonyan, D.; Fleischmann, C.; Vandervorst, W. Measurement of the Apex Temperature of a Nanoscale Semiconducting Field Emitter Illuminated by a Femtosecond Pulsed Laser. *J. Appl. Phys.* **2018**, *124*, 245105.
(32) Klingsporn, J. M.; Sonntag, M. D.; Seideman, T.; Van Duyne, R. P. Tip-Enhanced Raman Spectroscopy with Picosecond Pulses. *J. Phys. Chem. Lett.* **2014**, *5*, 106−110.
(33) Colomban, P.; Slodczyk, A. Raman Intensity: An Important Tool to Study the Structure and Phase Transitions of Amorphous/Crystalline Materials. *Opt. Mater.* **2009**, *31*, 1759−1763.
(34) Hart, T. R.; Aggarwal, R. L.; Lax, B. Temperature Dependence of Raman Scattering in Silicon. *Phys. Rev. B: Solid State* **1970**, *1*, 638−642.
(35) Richter, H.; Wang, Z. P.; Ley, L. The One Phonon Raman Spectrum in Microcrystalline Silicon. *Solid State Commun.* **1981**, *39*, 625−629.
(36) Doerk, G. S.; Carraro, C.; Maboudian, R. Temperature Dependence of Raman Spectra for Individual Silicon Nanowires. *Phys. Rev. B: Condens. Matter Mater. Phys.* **2009**, *80*, 073306.
(37) Wolf, I. D. Micro-Raman Spectroscopy to Study Local Mechanical Stress in Silicon Integrated Circuits. *Semicond. Sci. Technol.* **1996**, *11*, 139−154.
(38) Konstantinović, M. J.; Bersier, S.; Wang, X.; Hayne, M.; Lievens, P.; Silverans, R. E.; Moshchalkov, V. V. Raman Scattering in Cluster-Deposited Nanogranular Silicon Films. *Phys. Rev. B: Condens. Matter Mater. Phys.* **2002**, *66*, 161311.
(39) Zhen-Kun, L.; Yi-Lan, K.; Ming, H.; Yu, Q.; Han, X.; Hong-Pan, N. An Experimental Analysis of Residual Stress Measurements in Porous Silicon Using Micro-Raman Spectroscopy. *Chin. Phys. Lett.* **2004**, *21*, 403−405.
(40) Luft, A.; Franz, U.; Emsermann, L.; Kaspar, J. A Study of Thermal and Mechanical Effects on Materials Induced by Pulsed Laser Drilling. *Appl. Phys.* **1996**, *63*, 93−101.
(41) Ohmura, E.; Fukumitsu, K.; Morita, H. Internal Modified-Layer Formation Mechanism into Silicon with Nanosecond Laser. *J. Achiev. Mater. Manuf. Eng.* **2006**, *17*, 381−384. DOI: 10.1299/kikaic.74.446
(42) Gan, M.; Tomar, V. Surface Stress Variation as a Function of Applied Compressive Stress and Temperature in Microscale Silicon. *J. Appl. Phys.* **2014**, *116*, 073502.
(43) Meyer, J. R.; Bartoli, F. J.; Kruer, M. R. Optical Heating in Semiconductors. *Phys. Rev. B: Condens. Matter Mater. Phys.* **1980**, *21*, 1559−1568.
(44) Meyer, J.; Bartoli, F.; Kruer, M. Heating of Crystalline and Amorphous Silicon by C-Switched Laser Radiation. *J. Phys. Colloq.* **1980**, *41*, C4.
(45) Chen, X.; Wang, X. Near-Field Thermal Transport in a Nanotip under Laser Irradiation. *Nanotechnology* **2011**, *22*, 075204.
(46) Gao, J.; Xie, D.; Xiong, Y.; Yue, Y. Thermal Characterization of Microscale Heat Convection in Rare-Gas Environment by a Steady-State "Hot Wire" Method. *Appl. Phys. Express* **2018**, *11*, 066601.
(47) Wang, H.-D.; Liu, J.-H.; Guo, Z.-Y.; Zhang, X.; Zhang, R.-F.; Wei, F.; Li, T.-Y. Thermal Transport across the Interface between a Suspended Single-Walled Carbon Nanotube and Air. *Nanoscale Microscale Thermophys. Eng.* **2013**, *17*, 349−365.
(48) Klein, H. H.; Karni, J.; Ben-Zvi, R.; Bertocchi, R. Heat Transfer in a Directly Irradiated Solar Receiver/Reactor for Solid−Gas Reactions. *Sol. Energy* **2007**, *81*, 1227−1239.
(49) Ju, Y. S. Phonon Heat Transport in Silicon Nanostructures. *Appl. Phys. Lett.* **2005**, *87*, 153106.
(50) Park, Y.-H.; Kim, J.; Kim, H.; Kim, I.; Lee, K.-Y.; Seo, D.; Choi, H.-J.; Kim, W. Thermal Conductivity of Vls-Grown Rough Si Nanowires with Various Surface Roughnesses and Diameters. *Appl. Phys.* **2011**, *104*, 7.
(51) Martin, P.; Aksamija, Z.; Pop, E.; Ravaioli, U. Impact of Phonon-Surface Roughness Scattering on Thermal Conductivity of Thin Si Nanowires. *Phys. Rev. Lett.* **2009**, *102*, 125503.
(52) Alvarez, F. X.; Jou, D.; Sellitto, A. Phonon Boundary Effects and Thermal Conductivity of Rough Concentric Nanowires. *J. Heat Transfer* **2011**, *133*, 022402.